nature catalysis

ARTICLES

https://doi.org/10.1038/s41929-021-00665-3

Check for updates

Self-adaptive dual-metal-site pairs in metal-organic frameworks for selective CO_2 photoreduction to CH_4

Jian Li[1,3], Hongliang Huang[1,3], Wenjuan Xue[1,3], Kang Sun[2,3], Xiaohui Song[1], Chunrui Wu[1], Lei Nie[1], Yang Li[1], Chengyuan Liu[2], Yang Pan[2], Hai-Long Jiang[2]✉, Donghai Mei[1]✉ and Chongli Zhong[1]✉

Solar-light-driven reduction of CO_2-to-CH_4 is a complex process involving multiple elementary reactions and various by-products. Achieving high CH_4 activity and selectivity therefore remain a significant challenge. Here we show a bioinspired photocatalyst with flexible dual-metal-site pairs (DMSPs), which exhibit dynamic self-adaptive behaviour to fit mutative C1 intermediates, achieving CO_2-to-CH_4 photoreduction. The Cu and Ni DMSPs in their respective single-site forms under flexible microenvironment are incorporated into a metal-organic framework (MOF) to afford MOF-808-CuNi. This dramatically boosts CH_4 selectivity up to 99.4% (electron basis) and 97.5% (product basis), and results in a high production rate of 158.7 μmol g^{-1} h^{-1} with a sacrificial reagent. Density functional theory calculations reveal that the flexible self-adaptive DMSPs can stabilize various C1 intermediates in multistep elementary reactions, leading to highly selective CO_2-to-CH_4 process. This work demonstrates that efficient and selective heterogeneous catalytic processes can be achieved by stabilizing reaction intermediates via the self-adaptive DMSP mechanism.

The excessive combustion of fossil fuels is responsible for the excess emission of carbon dioxide (CO_2)[1–4]. It is becoming imperative to reduce the atmospheric CO_2 concentration. As a renewable C1 building block, CO_2 can be captured and converted into value-added fuels and chemicals as a sustainable mitigation method[5,6]. Among the CO_2 conversion pathways, the solar-light-driven conversion of CO_2 into valuable derivatives (for example, CO, CH_4 and HCOOH) is very promising[7–10]. Recent progress in photocatalytic CO_2 reduction is mainly related to the kinetically controlled two-electron products CO and HCOOH due to the high energy barriers of their further protonation processes[11–15]. Although CH_4 is a thermodynamically favoured product, the low activity and selectivity of CO_2 photoreduction to CH_4, which involves multiple proton-coupled electron transfer processes accompanied by various C1 intermediates on catalytic sites, remain a great challenge[16–19]. Therefore, developing a means of suppressing the kinetic products and manipulating the binding strengths between C1 intermediates and catalytic sites to access selective photocatalytic CO_2-to-CH_4 is of great significance.

Very recently, considering the synergetic effects of individual metal sites on reaction mechanisms, dual-metal sites in dinuclear metal complexes, carbon and other inorganic materials have been recognized to be an effective strategy for inducing high selectivity for desired products in multiple-step catalytic processes[16,20,21]. In particular, these dual-metal sites exhibit synergetic effects for bonding C1 intermediates to induce particular reaction paths in CO_2-to-CH_4 catalytic processes, providing a feasible way to improve CH_4 selectivity[18,19,22,23]. However, the reported dual-metal sites are generally located at fixed sites and consequently cannot provide suitable interactions with diverse intermediates in the overall CO_2-to-CH_4 process. When C1 intermediates escape from these stationary catalytic sites as a result of weak binding energy, undesired products will be generated, resulting in unsatisfactory selectivity to CH_4. In addition, from the activity perspective, the catalytic efficiency largely depends on the number of available catalytic sites. The number of accessible sites on a solid catalyst surface is usually limited in traditional photocatalysts, resulting in low CO_2-to-CH_4 activity.

To overcome the activity issue, good dispersion and accessibility of abundant dual-metal sites should be guaranteed in photocatalysts. For this purpose, it would be desirable to incorporate dual-metal-site pairs (DMSPs), in which each metal exists in its single-site form, into porous matrices. In this case, metal-organic frameworks (MOFs) would be ideal candidates[24–29]. MOFs featuring high porosity and surface area and sound CO_2 uptake capability can be easily modified with uniform sites, thereby bridging heterogeneous and homogeneous catalysis. Moreover, the Sabatier principle requires a moderate bonding strength between the catalyst (active site) and substrates (diverse intermediates in a multistep reaction). A three-dimensional active site could dynamically match with diverse intermediates, a motif observed in the special structural features of biological catalysts[30]. Therefore, DMSPs in flexible but not stationary microenvironment[31], mimicking the bonding with substrates and intermediates to induce suitable conformations in a natural enzyme system (induced fit)[32], would be highly desirable. Accordingly, the spatial configuration of such DMSPs in MOFs should be intelligently modulated to ensure their synergistic interactions with not only CO_2 molecules but also diverse C1 intermediates. It is expected that they should present self-adaptive behaviour (that is, active sites responsively evolve to stabilize mutative intermediates) and dynamic interactions to enable multiple elementary

[1]State Key Laboratory of Membrane Separation and Membrane Processes, School of Chemistry and Chemical Engineering, Tiangong University, Tianjin, China. [2]Hefei National Laboratory for Physical Sciences at the Microscale, Department of Chemistry, National Synchrotron Radiation Laboratory, University of Science and Technology of China, Hefei, Anhui, China. [3]These authors contributed equally: Jian Li, Hongliang Huang, Wenjuan Xue, Kang Sun. ✉e-mail: jianglab@ustc.edu.cn; dhmei@tiangong.edu.cn; zhongchongli@tiangong.edu.cn

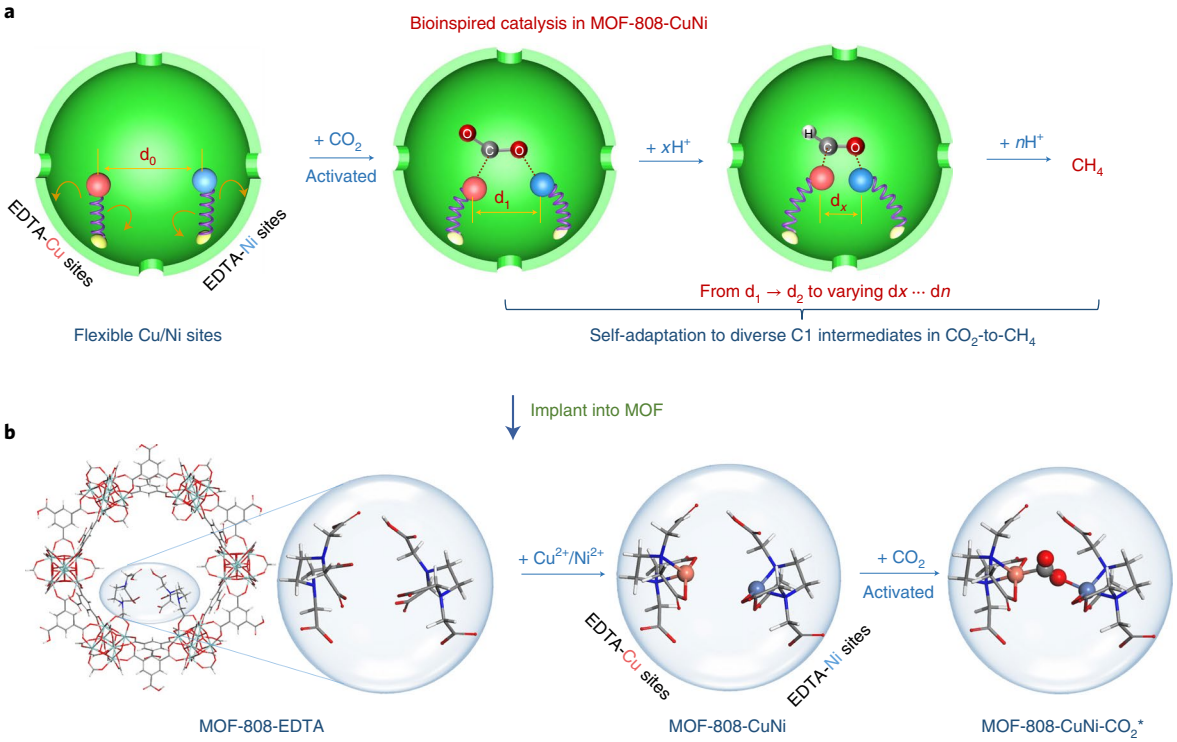

Fig. 1 | Schematic illustration of the self-adaptation concept. a,**b**, Implanting flexible and self-adaptive Cu/Ni DMSPs into MOF-808 for highly selective CO_2 photoreduction to CH_4. **a**, The flexible DMSPs for self-adaptive CO_2-to-CH_4 photoreduction. **b**, Schematic diagram of bioinspired CO_2 photoreduction in MOF-808-CuNi. Carbon, oxygen, hydrogen, nitrogen, copper and nickel atoms are coloured in grey, red, white, blue, orange and light-grey, respectively. The same colour scheme is applied in Figs. 2 and 5.

reactions, stabilizing the diverse C1 intermediates and suppressing by-products in the photocatalytic CO_2-to-CH_4 process. Although it is possible to precisely control the configurations between two single sites in MOFs thanks to their excellent structural tunability, to our knowledge, the creation of self-adaptive DMSPs in MOFs has not yet been reported.

Herein, DMSPs consisting of Cu and Ni in their respective single-site forms (referred to as Cu/Ni DMSPs) are incorporated into a robust MOF (namely, MOF-808), enabling free access to the sites to stabilize the various C1 intermediates in the photocatalytic CO_2-to-CH_4 process. To endow the metal sites with self-adaptive behaviour, flexible ethylenediaminetetraacetic acid (EDTA) was predangled onto the rigid Zr-oxo clusters, followed by metal chelation to yield MOF-808-CuNi. The resultant MOF-808-CuNi exhibits a high production rate of CH_4 (158.7 μmol g^{-1} h^{-1}) with an electron basis ($Sel_{electron}$) 99.4% (product basis ($Sel_{product}$) 97.5%) for CH_4. Density functional theory (DFT) calculations reveal that the synergistic effects and self-adaptive behaviour derived from the flexible DMSPs play crucial roles in stabilizing the diverse C1 intermediates, thereby suppressing undesired by-products and accounting for the high CH_4 selectivity.

Results

Morphological and structural characterization. The Cu/Ni DMSPs in MOF-808-CuNi were formed via a facile capture process, where Cu^{2+} and Ni^{2+} ions were chelated by the dangling EDTA ligands (Fig. 1a), where roughly two EDTA molecules are grafted onto each Zr_6 cluster (Fig. 1b and Supplementary Fig. 1). Powder X-ray diffraction patterns demonstrate their similar crystalline structures to MOF-808 (Supplementary Fig. 2)[33]. Although no Cu or Ni nanoparticles are present (Fig. 2a), the existence of Cu/Ni is demonstrated in MOF-808-CuNi (Fig. 2b,c, Supplementary Figs. 3 and 4 and Supplementary Note 1). The +2 oxidation states of Cu and Ni species in MOF-808-CuNi are further verified by X-ray photoelectron spectroscopy (XPS) (Supplementary Fig. 5). The shifted N 1*s* peak illustrates the strong interactions between Cu/Ni and the N atoms of EDTA (Supplementary Fig. 6).

To further unveil the status of Cu/Ni in MOF-808-CuNi, X-ray absorption near edge structure (XANES) profile was collected. It suggests that the Cu/Ni species are more positively charged than their metal foils and metal oxides, while they are more negatively charged than the metal ions (Supplementary Fig. 7a,b), possibly as a result of the chelation effect of the EDTA. The Fourier transforms of the extended X-ray absorption fine structure spectra exhibit an obvious Cu peak at roughly 1.47 Å and a Ni peak at roughly 1.69 Å, which are attributed to the isolated Cu(or Ni)-N(O) first coordination shell, whereas another minor peak at 2.17 Å (or 2.45 Å) could be ascribed to the Cu(or Ni)-C(N or O) second coordination shell (Fig. 2d,e). These results confirm that both Cu and Ni species are in their single-site forms in MOF-808-CuNi. The extended X-ray absorption fine structure fitting analyses further suggest that the Cu and Ni are chelated by EDTA with tetra-coordinated structures of Cu-2N-2O and Ni-2N-2O (Supplementary Fig. 8 and Supplementary Table 1), in line with the DFT-optimized results (insets, Fig. 2d,e and Supplementary Fig. 9a).

Given the nonconjugated structure of EDTA, it can endow the chelated Cu and Ni sites with dynamic behaviour. To further understand the bioinspired design of the flexible Cu/Ni DMSPs in MOF-808-CuNi, ab initio molecular dynamics (AIMD) simulations were carried out (Supplementary Video 1). Two important parameters, that is, the distance (d) between Cu and Ni atoms ($d_{Cu\text{-}Ni}$) and the dihedral angle (θ) formed by the four N atoms in EDTA ($\theta_{2N\text{-}2N}$), clearly describe the variable configurations and the dynamic local structure (Supplementary Fig. 9b,c). The values of $d_{Cu\text{-}Ni}$ and $\theta_{2N\text{-}2N}$

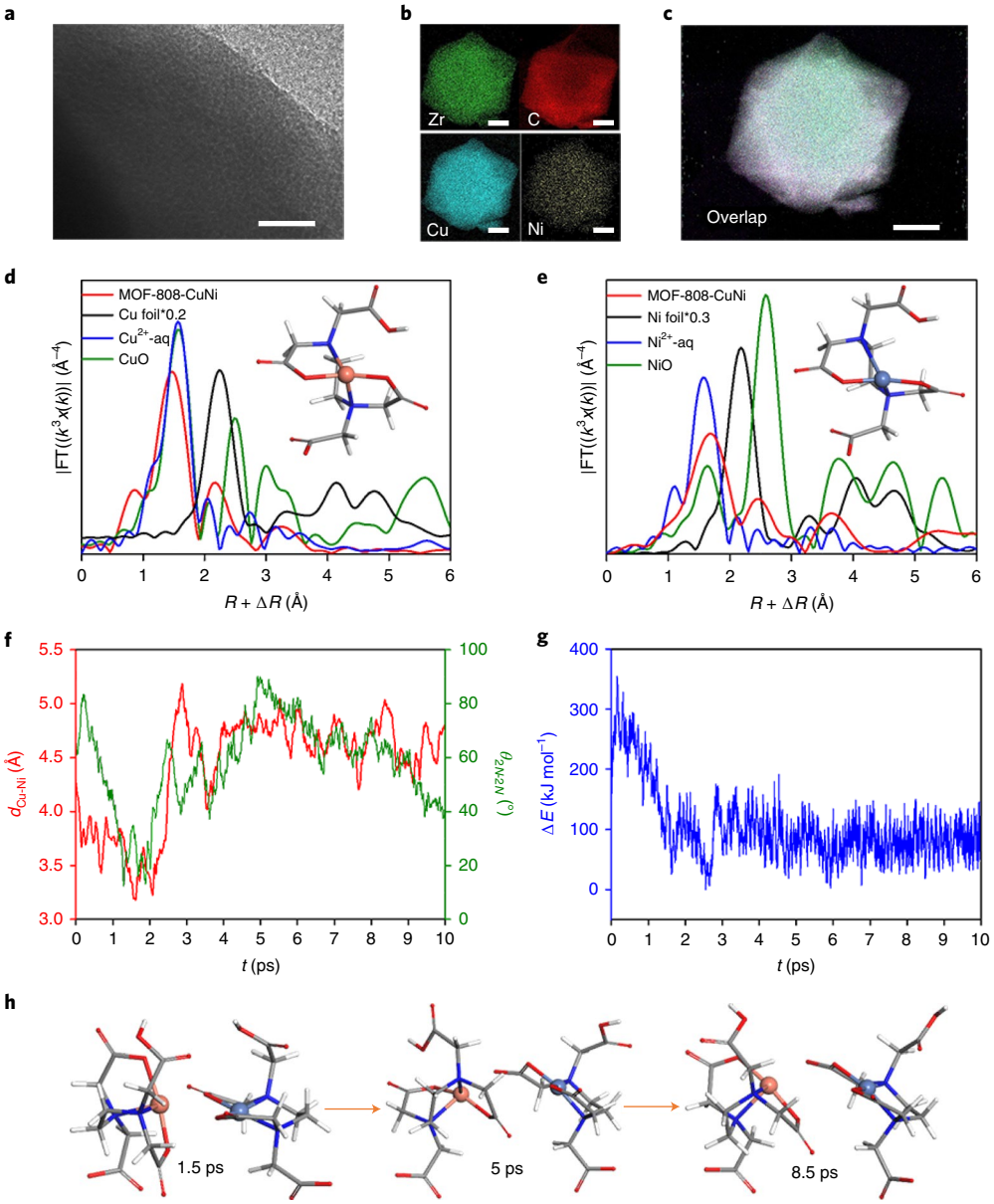

Fig. 2 | TEM observations and structural characterization of MOF-808-CuNi. a–**c**, HR-TEM image (scale bar, 20 nm) (**a**), energy-dispersive spectroscopy mapping (scale bar, 500 nm) (**b**) and elemental colour overlay images (scale bar, 500 nm) (**c**) of MOF-808-CuNi. **d**, Cu K-edge XANES spectra (inset, DFT-optimized structure of the Cu coordination sphere). **e**, Ni K-edge XANES spectra (inset, DFT-optimized structure of the Ni coordination sphere). **f**,**g**, AIMD-simulated $d_{Cu\text{-}Ni}$ and $\theta_{2N\text{-}2N}$ values for a Cu/Ni DMSP (**f**) and total energy changes relative to the minimum energy (ΔE) (**g**). *t*, time. **h**, Snapshot images of a flexible Cu/Ni DMSP recorded at 1.5, 5.0 and 8.5 ps (the Zr-oxo clusters and ligands in MOF-808-CuNi have been removed for clarity).

dynamically fluctuate in the ranges of 4.250 to 5.036 Å and 12.419° to 90.114°, respectively (Fig. 2f). Accordingly, the total energy also fluctuates throughout the AIMD simulations (Fig. 2g). Similar results can also be observed for MOF-808-Cu and MOF-808-Ni (Supplementary Fig. 10). More intuitively, randomly selected snapshot images recorded at 1.5, 5.0 and 8.5 ps show the different configurations of the Cu and Ni site pairs (Fig. 2h). These images unambiguously highlight the dynamic nature of the catalytic Cu/Ni DMSPs, which enables a bioinspired local structure, the spatial configuration of which can be self-regulated to adapt to diverse intermediates.

The loadings of Cu and Ni in MOF-808-CuNi are estimated to be 1.98 and 0.79 wt%, respectively (Supplementary Table 2). MOF-808-CuNi retains moderately high porosity, surface area and CO_2 uptake, indicating its sound CO_2 capture capability and accessibility (Supplementary Figs. 11–13). Also, MOF-808-CuNi possesses appropriate band edge positions for reducing CO_2 molecules (Supplementary Fig. 14 and Supplementary Note 2).

Selective photocatalytic conversion of CO_2 to CH_4. Photocatalytic CO_2 reduction reactions were conducted and described the Methods. As shown in Table 1 and Fig. 3a,b, MOF-808-EDTA exhibits CH_4, CO, H_2 and HCOOH evolution rates of 23.4, 3.4, 1.6 and 167.1 μmol g^{-1} h^{-1}, respectively, corresponding to low CH_4 selectivity. Evidently, the HCOOH evolution rate is much higher than that of CH_4. In comparison, the HCOOH evolution rate of 110.2 μmol g^{-1} h^{-1} over MOF-808-Ni presents only a slight decrease. This catalytic performance significantly changes after the Cu^{2+} incorporation. MOF-808-Cu displays an increased CH_4 production rate of 62.1 μmol g^{-1} h^{-1} and an effectively suppressed HCOOH

Table 1 | Photocatalytic CO_2 reduction performance over various catalysts

Entry[a]	Catalyst	Production rates (μmol g^{-1} h^{-1})				$Sel_{electron}$(%)[b]	$Sel_{product}$(%)[c]
		CH_4	CO	HCOOH	H_2		
1	MOF-808-CuNi	158.7	2.3	0	1.7	99.4	97.5
2	MOF-808-Cu	62.1	4.2	2.0	1.6	96.9	88.7
3	MOF-808-Ni	26.2	1.5	110.2	1.5	48.1	18.8
4	mix-MOF-808-Cu-Ni	47.7	2.6	78.2	1.8	69.8	36.6
6	MOF-808-EDTA	23.4	3.4	167.1	1.6	35.2	12.0

[a]Reaction conditions: 25 mg of catalyst and 50 mg (the molar concentration of 1.3 mM) of $[Ru(bpy)_3]Cl_2 \bullet 6H_2O$ as a photosensitizer; 30 ml of MeCN, 10 ml of TEOA as a sacrificial agent and 10 ml of H_2O; Visible light irradiation (420 nm < λ < 760 nm), 1 atm CO_2 and 25 °C. [b]Electron selectivity ($Sel_{electron}$) of CH_4: $Sel_{electron}(\%) = (8\,v(CH_4))/(8\,v(CH_4) + 2\,v(CO) + 2\,v(H_2) + 2\,v(HCOOH)) \times 100\%$; [c]Product selectivity ($Sel_{product}$) of CH_4: $Sel_{product}(\%) = (v(CH_4))/(v(CH_4) + v(CO) + v(H_2) + v(HCOOH)) \times 100\%$, where $v(CH_4)$, $v(CO)$, $v(H_2)$ and $v(HCOOH)$ denote the formation rates of CH_4, CO, H_2 and HCOOH, respectively.

production rate of 2.0 μmol g^{-1} h^{-1}. By integrating these two metals together to form DMSPs, a significantly enhanced CH_4 production rate of 158.7 μmol g^{-1} h^{-1} is achieved over MOF-808-CuNi, featuring turnover number of roughly 5.92 at 10 h based on Cu–Ni pairs. A high CH_4 $Sel_{electron}$ of roughly 99.4% and $Sel_{product}$ of roughly 97.5% is achieved, while the by-products are almost negligible. This finding indicates a synergistic effect between Cu and Ni sites for photoreducing CO_2 to CH_4. In contrast, photocatalytic CO_2 reduction over the physical mixture, denoted mix-MOF-808-Cu-Ni, yields a much inferior CH_4 evolution rate of 47.7 μmol g^{-1} h^{-1}. The MOF-808-CuNi(low), where the low metal loadings could increase the distance between Cu and Ni sites, exhibits low CH_4 selectivity (Supplementary Table 3), illustrating the synergistic effect might occur only between adjacent Cu and Ni sites. The homogeneous EDTA-CuNi also affords low activity and selectivity, highlighting the key role of MOF-808 for high performance. In particular, MOF-808-CuNi possesses superior CH_4 activity and selectivity, among MOF-808-MnCo, MOF-808-CuMn, MOF-808-NiCo and previously reported photocatalysts (Supplementary Tables 3 and 4). The CH_4 apparent quantum efficiency over MOF-808-CuNi (Supplementary Fig. 15 and Supplementary Note 3) is 2.31% under monochromatic light at 420 nm (ref. [34]). Moreover, the total electron transfer of MOF-808-CuNi reaches 1,277.6 μmol g^{-1} h^{-1}, much higher than that of other counterparts (Supplementary Table 5). To further verify the strong capabilities of MOF-808-CuNi for CO_2-to-CH_4 conversion, the use of CO and HCOOH in this photocatalytic system as C1 feeds was also attempted for generating CH_4. Explorative experiments were performed using CO and HCOOH feeds under an Ar atmosphere. As expected, MOF-808-CuNi exhibited a much higher CH_4 production rate than other catalysts, supporting the occurrence of a synergistic effect between Cu and Ni sites for photoreducing CO and HCOOH to CH_4 (Supplementary Fig. 16). The results indicate that the flexible DMSPs might self-adaptively bond various C1 intermediates during the reduction of CO_2 to CH_4. Control experiments clearly indicate that this is a real photocatalytic reduction process with triethanolamine (TEOA) as the sacrificial agent at 25 °C, the Ru complex as the photosensitizer and H_2O as the proton source (Fig. 3c, Supplementary Figs. 17 and 18 and Supplementary Notes 4 and 5). To explore the origin of the products, a $^{13}CO_2$ isotope labelling experiment over MOF-808-CuNi was conducted, demonstrating that CO_2 gas is responsible for the formation of carbon-related products (Fig. 3d,e). Photoelectrochemical measurements were performed to elucidate the excellent CO_2 photoreduction performance of MOF-808-CuNi. The photoluminescence peak intensity is slightly weakened after introducing Ni^{2+} ions and it is almost quenched on Cu^{2+} incorporation (Supplementary Fig. 19), suggesting that the incorporation of metal ions suppresses radiative electron-hole recombination[35]. Moreover, MOF-808-CuNi presents much better charge separation efficiency and lower charge transfer resistance than all other counterparts (Supplementary Figs. 20 and 21), demonstrating the superior separation and transport of photoinduced charges in MOF-808-CuNi, and this accounts well for its superior photocatalytic activity. Cycling experiments and heterogeneity tests demonstrate the reusable and heterogeneous nature of the catalysts; the activity and selectivity of MOF-808-CuNi are almost maintained in five consecutive runs (Supplementary Figs. 22–25 and Supplementary Note 6). The microstructure and situation of the catalyst can be retained during the reaction (Supplementary Figs. 26–28), demonstrating its stability. In addition, negligible poisoning effect excludes the formation of metal nanoparticles (Supplementary Fig. 29).

Charge transfer in the photocatalytic CO_2 reaction. To unveil the charge transfer behaviour during the photocatalytic CO_2 reaction over MOF-808-CuNi, electron spin resonance (ESR) measurements were conducted. The ESR peak (Supplementary Fig. 30) of MOF-808-EDTA at $g = 2.002$ is assignable to oxygen-centred active sites in Zr-oxo clusters[36–40], which is generated by electron transfer from $[Ru(bpy)_3]Cl_2$ to Zr-oxo clusters in the MOF. This ESR signal becomes much weaker under a CO_2 atmosphere as electrons are transferred to CO_2 from Zr-oxo centres. Given that Cu(I) and Ni(II) do not generate ESR signals[41,42], the apparent ESR peaks at $g = 2.044$ and 2.115 are ascribed to Cu(II) and Ni(I), respectively (Fig. 4a,b). On light irradiation, the signal of Cu(II) displays an evident decrease, accompanied by the appearance of the Cu(I) peak in the Auger spectrum (Supplementary Fig. 31 and Supplementary Note 7), while the Ni(I) signal is enhanced indicating that both metal sites are able to accept electrons from Zr-oxo clusters in MOF-808-CuNi. When CO_2 is introduced into the system, these ESR signals are partially recovered, clearly disclosing electron migration from metal sites to CO_2, giving rise to its subsequent reduction. DFT calculations show the charge density differences between the MOF-808-CuNi system and MOF-808-CuNi system with CO_2 (Fig. 4c,d), further emphasizing that electrons are transported from Zr-oxo clusters to Cu/Ni DMSPs and then coupled with CO_2 molecules.

With the above results, the charge transfer mechanism underlying the CO_2 photoreduction over MOF-808-CuNi can be illustrated (Fig. 4e). On photoexcitation, $[Ru(bpy)_3]^{2+}$ is promoted to the excited state. This excited state is directly quenched, accompanied by the $[Ru(bpy)_3]^{3+}$ formation, during which electrons are transferred from the Ru complex to Zr-oxo clusters. The oxidized light absorber is reduced back to $[Ru(bpy)_3]^{2+}$ with the help of TEOA. Then, the electrons on Zr-oxo clusters briefly migrate to Cu/Ni DMSPs. Once CO_2 molecules interact with Cu/Ni DMSPs, the electrons are transferred to CO_2, leading to the CH_4 product.

Reaction mechanism of CO_2 photoreduction to CH_4. In situ diffuse reflectance infrared Fourier transform spectroscopy (DRIFTS)

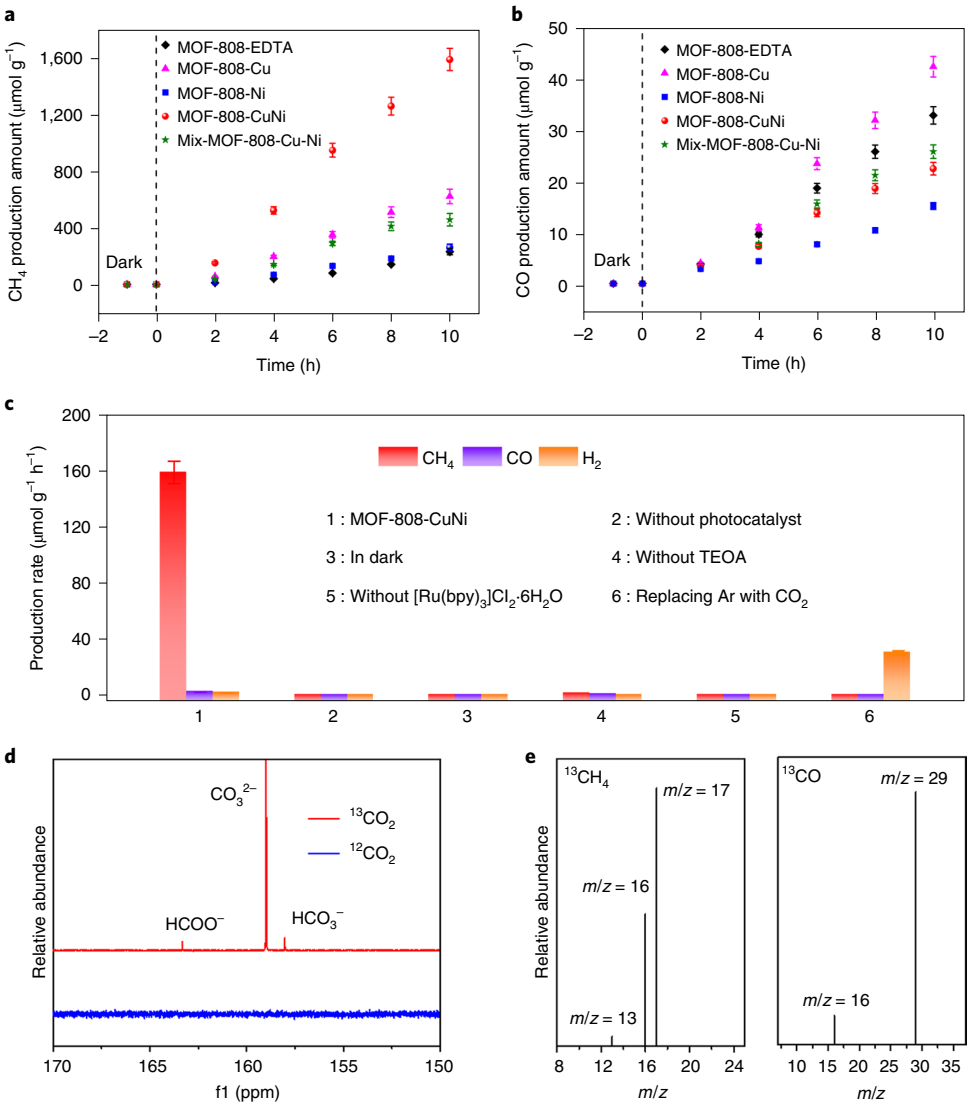

Fig. 3 | Photocatalytic CO_2 reduction performance. a,**b**, Time-dependent CH_4 and CO evolution curves. Time-dependent production of CH_4 (**a**) and CO (**b**) under visible light irradiation (420 nm < λ < 760 nm) within 10 h using MOF-808-EDTA (black diamond), MOF-808-Cu (pink triangle), MOF-808-Ni (blue square), MOF-808-CuNi (red sphere) and mix-MOF-808-Cu-Ni (green star). **c**, The control experiments of photocatalytic CO_2 reduction performance over MOF-808-CuNi under altered conditions; error bars mean ± standard deviations calculated from three independent measurements. **d**,**e**, The isotope labelling experiment for HCOOH, CH_4 and CO. **d**, ^{13}C nuclear magnetic resonance spectra of the HCOOH product obtained from reaction over MOF-808-EDTA with $^{13}CO_2$ and $^{12}CO_2$. **e**, Mass spectra of $^{13}CH_4$ (m/z = 17) and ^{13}CO (m/z = 29) produced in the photocatalytic reduction of $^{13}CO_2$ over MOF-808-CuNi.

was performed to detect the reaction intermediates in photocatalytic CO_2 reduction (Fig. 5a and Supplementary Fig. 32). The peaks at 1,439, 1,510 and 1,676 cm^{-1} can be assigned to HCO_3*, CO_3* and CO_2* species, respectively, which are generated from CO_2 and −OH groups and might serve as possible intermediates for subsequent production of C1 fuels[43]. The CO* absorption band at 2,077 cm^{-1} can be observed in the photocatalytic process[44]. Considering this, the trace amount of CO generated in this photocatalytic system is understandable. The bands at 1,135 and 1,377 cm^{-1} assignable to OCH_3* and CH_3* groups, respectively, are recognized as the key intermediates that are directly related to the CO_2-to-CH_4 photoreduction[43,45].

To further understand the CO_2 photoreduction over MOF-808-CuNi, DFT calculations were conducted to illustrate the critical role of the flexible Cu/Ni DMSPs in achieving the excellent CH_4 selectivity. As shown in Fig. 5b (Supplementary Figs. 33–36, Supplementary Notes 8 and 9 and Supplementary Table 6), CO_2 photoreduction over MOF-808-CuNi follows the COOH* intermediate route, which is first triggered by the activation of CO_2* with Cu-C and Ni-O bonds. Although both CO_2* protonation steps are endergonic (+5 and +23 kJ mol^{-1}), the first protonation step of CO_2* leading to the COOH* formation is thermodynamically and kinetically more feasible than the HCOO* formation, with the Gibbs free energy of activation of 54 versus 115 kJ mol^{-1}. The protonation of formed COOH* produces HCOOH* with a large exergonic reaction energy (−83 kJ mol^{-1}). Another reaction path for COOH* protonation leads to the CO* formation, with an exergonic Gibbs free reaction energy of −21 kJ mol^{-1}. Although the HCOOH formation is thermodynamically more favourable, DFT calculations show the CO* formation is spontaneous while the HCOOH* formation needs to overcome a kinetic barrier of 63 kJ mol^{-1}. The desorption of HCOOH* and CO* from the Cu/Ni DMSPs is difficult because the large desorption energies of +94 and +65 kJ mol^{-1}, respectively. This is consistent with our experimental observation of very

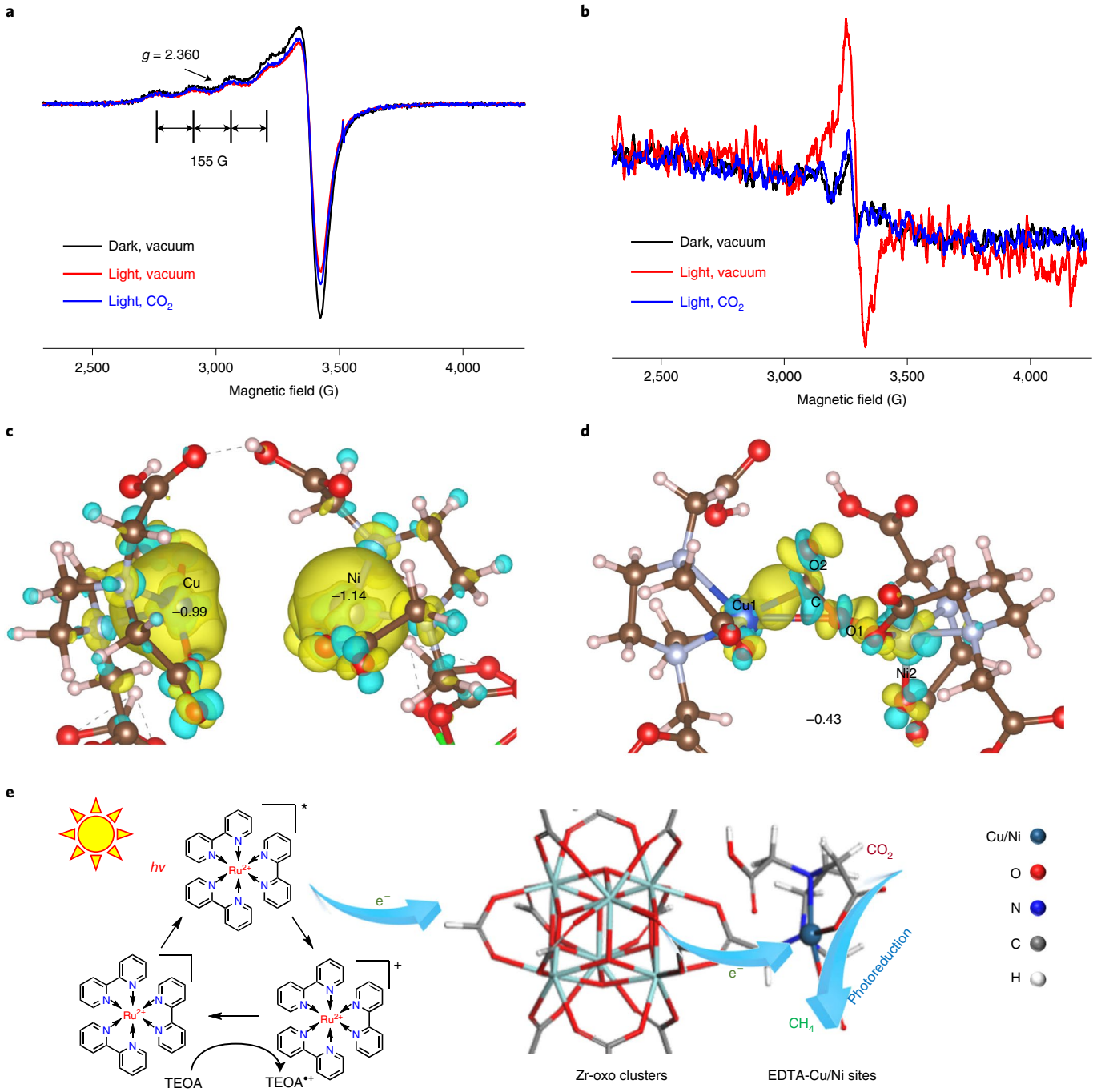

Fig. 4 | Charge transfer in CO_2 photoreduction over MOF-808-CuNi. a,**b**, ESR spectra of Cu species in MOF-808-CuNi (**a**) and Ni species in MOF-808-Ni (**b**) (MOF-808-Ni is studied instead here because the Ni signal is shielded by the strong Cu signal in MOF-808-CuNi) under various conditions. The $A_{//}$ of 155 G for Cu and the $g_{//}$ of 2.360 are for the distorted tetrahedral Cu coordination, where // indicates that coordinate axes are parallel to the magnetic direction. **c**, Isosurfaces (level 0.005) of charge density differences on MOF-808-EDTA with Cu^{2+} and Ni^{2+}. The minus sign indicates electron accumulation. **d**, Isosurfaces (level 0.005) of charge density differences on MOF-808-CuNi with CO_2 molecules. Yellow indicates electron accumulation, and light blue indicates depletion. **e**, Schematic process of charge transfer in the photocatalytic CO_2 reaction over MOF-808-CuNi using $[Ru(bpy)_3]Cl_2 \bullet 6H_2O$ as a photosensitizer (the ligands in MOF-808-CuNi are removed for clarity).

low CO production rate (2.3 μmol g^{-1} h^{-1}) and no HCOOH product. With calculated Gibbs free energies, CO hydrogenation over MOF-808-CuNi is much faster than its desorption, substantially inhibiting CO desorption. The formed CO* is further converted into HCO* with a small energy barrier of 39 kJ mol^{-1}, while the conversion of HCOOH*-to-HCO* step is not feasible due to the high Gibbs free energy of activation of 91 kJ mol^{-1}. On HCO* formation, the subsequent two protonation steps leading to the methoxy (H_3CO*) formation are kinetically relevant with Gibbs free energies of activation of 51 and 69 kJ mol^{-1}, respectively. Then, the CH_3OH* intermediate is formed with an exergonic of −18 kJ mol^{-1} conquering a barrier of 50 kJ mol^{-1}. DFT calculation also suggests CH_3OH desorption is difficult because of the large desorption energy of +174 kJ mol^{-1}. The formed CH_3OH* is then further dehydrated into

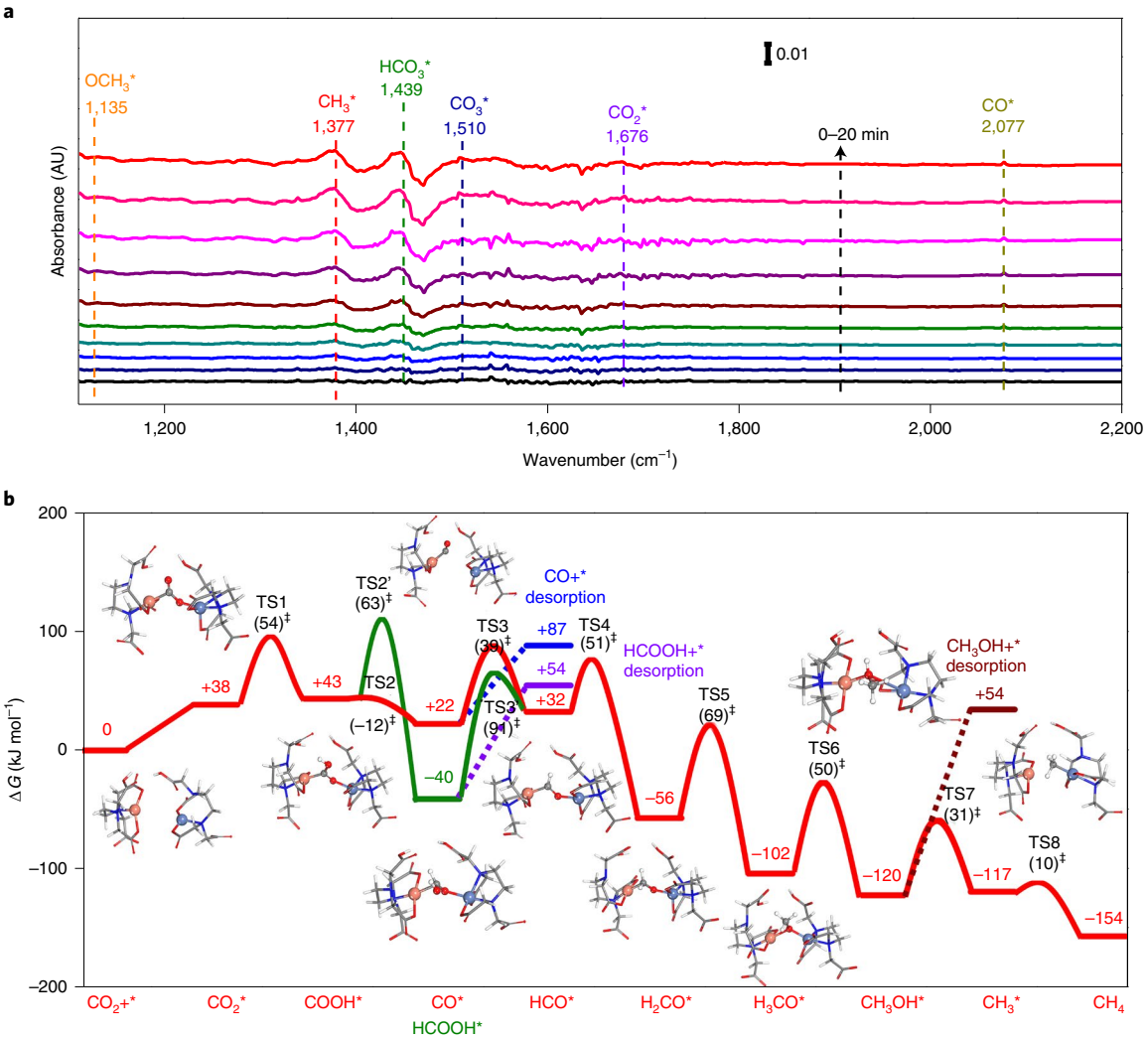

Fig. 5 | Detection of the reaction mechanism for the photoreduction of CO_2 to CH_4. a, In situ DRIFTS spectra at 1,110–2,200 cm^{-1} for detecting the reaction intermediates in CO_2 photoreduction and recording the adsorption and activation of CO_2 over MOF-808-CuNi in the presence of H_2O under visible light irradiation. AU, arbitrary units. **b**, Gibbs free energy diagram. The energy data (in red) are the energy of each intermediate state, which is relative to the energy (zero) of the reference system, that is, MOF-808-CuNi and gaseous CO_2. The energy data in brackets (in black) are the calculated Gibbs free energy of activation for each elementary step.

the CH_3*. Significantly, the generation of CH_3* is evidenced by the in situ DRIFTS results, confirming that CH_4 is derived from CH_3*.

For comparison, we also calculated the Gibbs free energy diagrams of CO_2 photoreduction over MOF-808-Cu and MOF-808-Ni on the assumption of the similar reaction route over MOF-808-CuNi (Supplementary Figs. 37–42). For MOF-808-Ni, Gibbs free energies of activation for the formation of CO* and HCOOH* from COOH* are 70 and 72 kJ mol^{-1}, respectively, indicating these two key reaction steps are competitive. Since the calculated Gibbs free reaction energy of −21 kJ mol^{-1} and no transition state is located, the desorption of the formed HCOOH* is spontaneous. Given the conversion of HCOOH* to HCO* has to overcome a Gibbs free energy of activation of 46 kJ mol^{-1}, the formed HCOOH* would desorb rather than further being converted leading to CH_4 formation. This explains the experimentally observed high HCOOH production rate of 130.2 μmol g^{-1} h^{-1} over MOF-808-Ni, and HCOOH rather than CH_4 becomes the main product. Conversely, DFT calculation results show the CO* formation from COOH* is more favourable than the HCOOH* formation over MOF-808-Cu. Although the HCO* formation by CO* protonation has a large free energy barrier of 70 kJ mol^{-1}, the CO desorption barrier of +76 kJ mol^{-1} is higher. Therefore, the formed CO* will be further protonated until the CH_4 formation on MOF-808-Cu. Although the same main product of CH_4 was observed for both MOF-808-CuNi and MOF-808-Cu, compared with MOF-808-CuNi, the CH_4 production rate (62.1 μmol g^{-1} h^{-1}) over MOF-808-Cu is greatly reduced. This is largely due to the higher activation barrier of 84 kJ mol^{-1} for CO_2* activation on MOF-808-Cu than that of 54 kJ mol^{-1} on MOF-808-CuNi, which is consistent with our experimental observation. Furthermore, the calculated time of flight for the CO_2-to-CH_4 photoreduction of over MOF-808-CuNi is much higher than those over MOF-808-Cu and MOF-808-Ni (Supplementary Tables 7 and 8 and Supplementary Note 10).

Self-adaptive Cu/Ni DMSPs in MOF-808-CuNi. To reveal the role of self-adaptive Cu/Ni DMSPs in the CO_2 photoreduction over MOF-808-CuNi, the optimized catalyst structures were also analysed by the key structural parameters $d_{Cu\text{-}Ni}$ and $\theta_{2N\text{-}2N}$ (Fig. 6a,b and Supplementary Fig. 34). The original $d_{Cu\text{-}Ni}$ before a CO_2 molecule is adsorbed onto the catalyst is 4.312 Å, while this

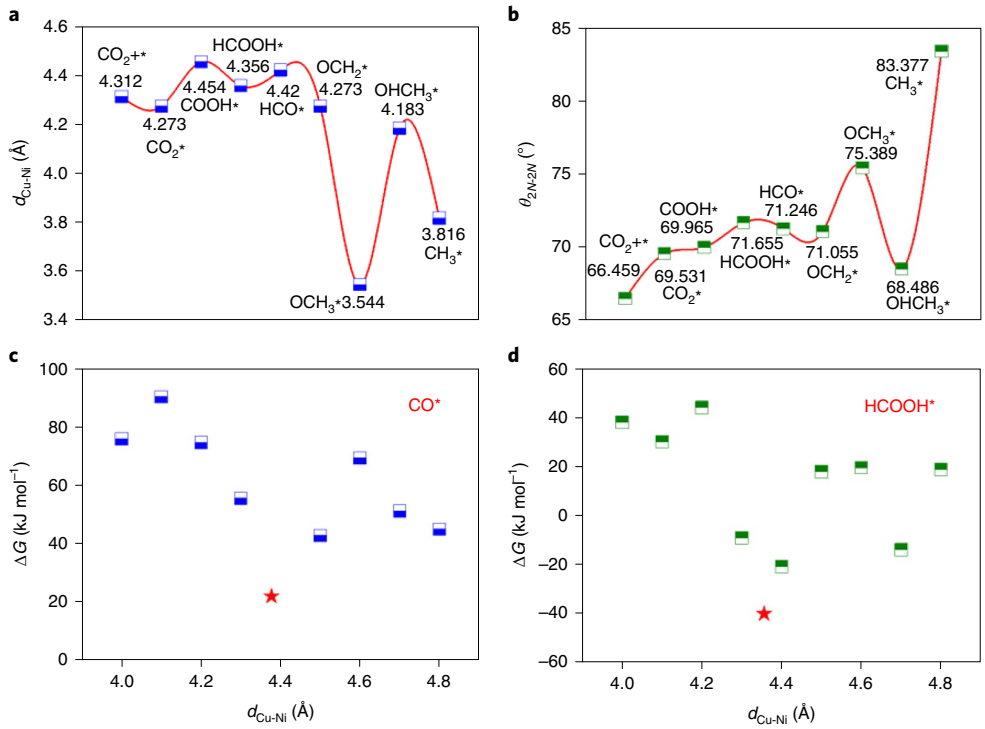

Fig. 6 | Self-adaptive Cu and Ni sites for the selective photoreduction of CO_2 to CH_4. a,b, Configuration evolution with varying values of d_{Cu-Ni} (**a**) and θ_{2N-2N} (**b**). **c,d**, Adsorption energies of CO* (**c**) and HCOOH* (**d**) intermediates for various Cu/Ni distances. The red asterisks (*) represents the strongest binding energies for the CO* and HCOOH* intermediates that are found with the self-adaptive flexible d_{Cu-Ni} distance.

value is adjusted to 4.454 Å to accommodate COOH* after one proton-coupled electron transfer process (Fig. 6a). When COOH* evolves into HCOOH* via the next hydrogenation step, the d_{Cu-Ni} value changes to 4.356 Å. Similarly, the other important parameter, θ_{2N-2N}, ranges from 66.459° to 83.377° during the CO_2 photoreduction process (Fig. 6b). Clearly, the spatial configuration of the Cu/Ni DMSP is dynamic during CO_2 photoreduction process. Just like the most suitable configurations of enzymes can be induced by bonding to substrates[46], the d_{Cu-Ni} and θ_{2N-2N} values continuously evolve to stabilize the C1 intermediates, suppressing the desorption of by-products. This is believed to be the origin of the highly selective photoreduction of CO_2 to CH_4. In this way, it can be expected that each reaction intermediate will be in its optimal state during the CO_2 photoreduction reaction. To further prove this assumption, the binding energies of CO* and HCOOH* on a self-adaptive Cu/Ni DMSP are compared with those for static Cu/Ni site pairs with ten different fixed Cu–Ni distances ranging from 4.0 to 4.8 Å (Fig. 6c,d). Both CO* and HCOOH* are found to have the strongest binding energies for the self-adaptive Cu/Ni DMSP. Therefore, both CO* and HCOOH* will remain at self-adaptive Cu/Ni DMSPs for further protonation without desorption. We believe that this enhanced stabilization of each reaction intermediate, enabled by the self-adaptive Cu/Ni DMSPs, is the critical factor in achieving the very high CH_4 activity and selectivity.

Conclusions

In summary, we have developed a MOF photocatalyst featuring Cu/Ni DMSPs, which exhibit the dynamic capability of enzymes to self-adaptively stabilize diverse C1 intermediates during CO_2 photoreduction, thereby significantly boosting the activity and selectivity for CH_4. Both Cu and Ni exist in their single-site forms and flexible microenvironment in the DMSPs incorporated into the MOF skeleton[29], and the bioinspired design of these Cu/Ni DMSPs is confirmed by AIMD simulations. Moreover, DFT calculations unambiguously suggest the synergistic mechanism, in which the spatial configurations of the Cu/Ni DMSPs evolve continuously with the diverse C1 intermediates in a self-adaptive manner during the multistep photocatalytic CO_2 reduction. As a consequence, MOF-808-CuNi exhibits a high $Sel_{electron}$ of roughly 99.4% and $Sel_{product}$ of roughly 97.5% with a fast yield of 158.7 μmol g^{-1} h^{-1}. This work, inspired by enzymes, provides an approach for the fabrication of heterogeneous catalysts featuring self-adaptive DMSPs for stabilizing reactive intermediates toward efficient and selective CO_2 photoreduction.

Methods

Synthesis of catalysts. *MOF-808-CuNi.* The MOF-808 and MOF-808-EDTA were prepared according to the previously reported methods with modifications[47,48]. Typically, MOF-808 was prepared by 1,3,5-benzenetricarboxylic acid (H_3BTC) and $ZrOCl_2$•$8H_2O$ in a solvent mixture of DMF/formic acid at 135 °C for 48 h. EDTA was dangled onto Zr-oxo clusters by reacting MOF-808 in EDTA-2Na aqueous solution at 60 °C for 24 h. Then Cu^{2+} and Ni^{2+} ions were tethered to MOF-808-EDTA by a facile adsorption and chelation process. Specifically, 100 mg of MOF-808-EDTA was dispersed in 100 ml of aqueous solution with 10 mg of $Ni(NO_3)_2$•$6H_2O$ and 8 mg of $Cu(NO_3)_2$•$3H_2O$, and reacted by stirring for 12 h at 25 °C. The product was washed with water and centrifugated, followed by drying under vacuum at 60 °C to afford MOF-808-CuNi.

MOF-808-Cu. Following a similar synthetic procedure to that of MOF-808-CuNi, the MOF-808-Cu was prepared by using 16 mg of $Cu(NO_3)_2$•$3H_2O$, without any other metal salt.

MOF-808-Ni. Following a similar synthetic procedure to that of MOF-808-CuNi, the MOF-808-Ni was prepared using 20 mg of $Ni(NO_3)_2$•$6H_2O$, without any other metal salt.

Mix-MOF-808-Cu-Ni. The 100 mg of physical mixture was obtained by physically mixing 50 mg of MOF-808-Cu and 50 mg of MOF-808-Ni.

MOF-808-CuNi(low). The MOF-808-CuNi(low) was prepared following a similar synthetic procedure to that of MOF-808-CuNi, except for using 0.5 mg of $Ni(NO_3)_2$•$6H_2O$ and 0.4 mg of $Cu(NO_3)_2$•$3H_2O$, without any other metal salt.

MOF-808-MnCo. The MOF-808-MnCo was prepared following a similar synthetic procedure to that of MOF-808-CuNi, except for using 9 mg of $Mn(NO_3)_2{\bullet}4H_2O$ and 10 mg of $Co(NO_3)_2{\bullet}6H_2O$, without any other metal salt.

MOF-808-CuMn. The MOF-808-CuMn was prepared following a similar synthetic procedure to that of MOF-808-CuNi, except for using 9 mg of $Mn(NO_3)_2{\bullet}4H_2O$ instead of 10 mg of $Ni(NO_3)_2{\bullet}6H_2O$.

MOF-808-NiCo. The MOF-808-NiCo was prepared following a similar synthetic procedure to that of MOF-808-CuNi, except for using 10 mg of $Co(NO_3)_2{\bullet}6H_2O$ instead of 8 mg of $Cu(NO_3)_2{\bullet}3H_2O$.

EDTA-CuNi. Typically, 40 mg of EDTA-2Na (on the basis of the amount of EDTA in MOF-808-EDTA) was stirred in 100 ml of aqueous solution with 10 mg of $Ni(NO_3)_2{\bullet}6H_2O$ and 8 mg of $Cu(NO_3)_2{\bullet}3H_2O$ for 12 h at 25 °C. The product was obtained by the evaporation of water.

Characterization. A JEOL JEM-2100 with energy-dispersive spectroscopy elemental mapping and JEM-ARM200F transmission electron microscopy (TEM)/scanning TEM (STEM) equipment were used to record high-resolution–TEM (HR–TEM) and high-angle annular dark-field scanning TEM images, respectively. Autosorb-IQ-MP Quantachrome Instruments were applied in gas sorption curves at 77 K. Powder X-ray diffraction data were measured at an X-ray diffractometer (BRUKER D2 PHASER). The XPS and Auger electron spectroscopy data were collected by ESCALAB 250 X-ray photoelectron spectrometer and the excitation source is Al Kα X-ray. The position of C 1*s* line at 284.6 eV was used to correct all XPS spectra. In situ DRIFTS spectra were collected on a Nicolet iS 10 Fourier transform infrared spectrometer equipped with a mercury cadmium telluride detector, using two CaF_2 as windows with the humid ultra-pure CO_2 (99.999%) under visible light irradiation. The flowing CO_2 gas passes through the H_2O trap, before going into the in situ DRIFTS instrument. To avoid the signals of organic ligand, the in situ DRIFTS data were analysed by the difference value of 0 min in light. The Cu and Ni contents were determined by inductively coupled plasma–mass spectrometry data analysis. A Bruker Fourier 400M was used to test nuclear magnetic resonance. The Shimadzu UV-3101 spectrophotometer was used to record UV-vis diffuse reflection spectra. The X-ray absorption structures at the Cu and Ni K-edge of the MOF-808-CuNi were obtained in fluorescence excitation mode using a Lytle detector at the 1W1B station at the Beijing Synchrotron Radiation Facility and the double crystal monochromator was silicon (111). k^3-weighted $\chi(k)$ data in the *k*-space were Fourier-transformed to real (R) space using a Hanning windows to separate the EXAFS contributions from different coordination shells. ESR data were recorded on a JEOL JES-FA200 EPR spectrometer under irradiation with a xenon lamp. Synchrotron-radiation vacuum ultraviolet photoionization–mass spectrometry was conducted at the combustion endstation of the BL03U beamline in the organization of Hefei National Synchrotron Radiation Laboratory at 14 eV for detecting D_2O and CO_2 products.

Photocatalytic CO_2 reduction measurements. Here, 25 mg of photocatalyst powder and 50 mg (molar concentration 1.3 mM) of $[Ru(bpy)_3]Cl_2{\bullet}6H_2O$ were mixed in a 50-ml solution containing 30 ml of acetonitrile, 10 ml of TEOA and 10 ml of H_2O in a 250-ml quartz reaction cell. The CO_2 (purity >99.999%) was purged into this reaction cell for 0.5 h to eliminate the dissolved oxygen. Before illumination, the reactor was installed to CEL-SPH2N system (Beijing China Education Au-light Co., Ltd) equipped with a 300-W Xe lamp with the 420-nm cutoff filter ($420\,nm < \lambda < 760\,nm$). On degassing, the system was filled with CO_2 (purity >99.999%) to 1 atm. For photocatalytic CO and HCOOH reduction measurements, 10 ml of CO (99.999%) or 1 ml of liquid HCOOH was injected into photocatalytic system. Subsequently, the Ar as the packed gas was purged into the system to reach atmospheric pressure. Gas chromatography (Agilent 7890B) was applied to analysed gaseous products by the detectors of a thermal conductivity detector and a flame ionization detector using Ar as the carrier gas. The HCOOH in the liquid phase was analysed using ion chromatography (Thermo ICS-5000). The possible alcohol products were detected by a liquid chromatogram (Waterse 2695), and no related signals could be observed. The catalytic results were repeated three times with three batches of catalysts to give more reliable data. Gas chromatography–mass spectrometry (Bruker solanX 70 FT-MS) was applied to analyse the isotope labelled products using $^{13}CO_2$ as the feed gas. The light intensity data were measured using a PM100D optical power meter (Thorlabs) equipped with a S425C detector (Supplementary Table 9). The heterogeneity test was performed by removing the catalyst from the reaction medium at 6 h by centrifugation[49].

Photoelectrochemical measurements. The CHI760E electrochemical workstation (Shanghai Chenhua Instrument Co., Ltd, China) was used to conduct photoelectrochemical measurements in 0.5 $mol\,l^{-1}$ Na_2SO_4 solution with a 300-W Xe lamp light source. A three-electrode experimental system contained the counter electrodes (Pt foil), reference electrodes (Ag/AgCl) and working electrodes (as-prepared catalysts). The photocurrent was performed by intermittent illumination with 0.5 V bias. Electrochemical impedance spectra were measured at open circuit potential. Mott–Schottky plots were measured at the frequencies of 1,000, 2,000 and 3,000 Hz.

The CH_4 yields were measured using 420-nm monochromatic light, and the apparent quantum efficiency (AQE) (Supplementary Fig. 15) was calculated on the basis of Ferrioxalate actinometry[34].

The total transferred electrons were calculated as follows,

$$\text{Total electron transfer} = 2 \times \text{CO production rate} + 8 \times \text{CH}_4\text{ production rate} + 2 \times \text{HCOOH production rate} + 2 \times \text{H}_2\text{ production rate} \quad (1)$$

First-principles-based computational details. All DFT calculations were carried out in the framework of the CP2K code with mixed Gaussian and plane-wave basis sets[50]. The norm-conserving Goedecker–Teter–Hutter pseudopotentials were used to describe the core electrons[51–54]. The valence electron wave function was expanded in a double-ζ basis set with polarization functions[55] along with an auxiliary plane-wave basis set. The Perdew, Burke and Enzerhof exchange-correlation functional[56] within the generalized gradient approximation was adopted in the calculations. The cutoff energy was set to 360 Ry. The Γ-point only sampling scheme was applied in all calculations. To verify the calculation accuracy, each reaction configuration was optimized using the Broyden–Fletcher–Goldfarb–Shanno algorithm with self-consistent field convergence criteria of 1.0×10^{-8} AU. The total energy change of the reaction configuration was negligible (<0.01 eV) when the force convergence criteria of 0.001 hartree per bohr was used. The compensation for the long-range van der Waals dispersion interaction between the adsorbates and MOF skeleton was described using the DFT-D3 scheme[57] with an empirical damped potential term.

The Gibbs free reaction energy for each elementary step was calculated at 298.15 K using the computational hydrogen electrode model:[58,59]

$$\Delta G = \Delta E_{\mathrm{DFT}} + \Delta E_{\mathrm{ZPE}} - T\Delta S + \sum eU \quad (2)$$

where ΔE is the difference of electronic energy derived from CP2K, ΔE_{ZPE} is the difference of zero-point energy (ZPE) and $T\Delta S$ is the entropy change, as shown in Supplementary Table 10; *e* is the elementary charge, $\sum e$ is the number of transferred electrons and *U* is the applied overpotential, where $U = 0$ V, that is, zero overpotential referenced with the reversible hydrogen electrode and non-charged models are applied in this work. The reliability of non-charged calculation system in the computational hydrogen electrode model has also been investigated in photoelectrochemical reduction of CO_2 to CH_4 (Supplementary Figs. 43 and 44, Supplementary Tables 11 and 12 and Supplementary Notes 11 and 12). The CO hydrogenation rate constant k_{HYD} and CO desorption rate constant k_{DES} are 0.018 and $4.81\times10^{-12}\,s^{-1}$, respectively. E_{ZPE} and *TS* for each reaction intermediate were calculated as follows[60],

$$E_{\mathrm{ZPE}} = \frac{1}{2}\sum_i h\nu_i \quad (3)$$

$$-TS = k_{\mathrm{B}}T\sum_i \ln\left(1 - \mathrm{e}^{-\frac{h\nu_i}{k_{\mathrm{B}}T}}\right) - \sum_i h\nu_i\left(\frac{1}{\mathrm{e}^{\frac{h\nu_i}{k_{\mathrm{B}}T}} - 1}\right) \quad (4)$$

where *h*, ν_i and k_{B} are the Planck constant, vibrational frequency and Boltzmann constant. Please note only the adsorbates, Cu and Ni atoms were taken into account in the vibrational frequency calculations, while the contributions from the MOF-808-EDTA framework were assumed to be negligible. Gibbs free energies of activation for each elementary step were calculated using the climbing image nudged elastic band method[61,62]. Supplementary Tables 13–15 show the DFT calculated ΔTS, ΔE_{ZPE}, ΔE_{DFT} and ΔG (all in kJ mol^{-1}) for reaction intermediates over MOF-808-CuNi, MOF-808-Cu and MOF-808-Ni. The pristine MOF-808 was composed of $Zr_6O_4(OH)_4(HCOO)_6$ metal nodes, where each metal node was connected with six 1,3,5-benzene tricarboxylate (BTC^{3-}) ligands. The diameter of MOF-808 pore apertures was 14 Å. The periodic MOF-808 unit cell had 1,280 atoms with a lattice constant of 35.0764 Å (Supplementary Fig. 45). To identify the structure of the self-adaptive DMSPs, three configurations with *ortho*, *meta* and *para* positions of two EDTA ligands anchored single Ni and Cu atoms in the six-ring pore of the MOF-808 framework were initially set up, as shown in Supplementary Fig. 46. Periodic AIMD simulations of MOF-808-CuNi were performed in the canonical ensemble (NVT) at 300 K using CP2K. The Nosé–Hoover thermostat method was implemented in the NVT ensemble simulations with the time step of 0.5 fs. Each AIMD simulation was run for 20,000 steps, that is a total simulation time of 10 ps. AIMD simulations show that the neighbouring EDTA ligands in the ortho position provide the self-adaptive DMSPs. For computationally feasible, a MOF-808-CuNi cluster model was built in the calculations for studying reaction mechanism and dynamic feature of self-adaptive DMSPs. As shown in Supplementary Fig. 9a, the MOF-808-CuNi cluster model with a total of 276 atoms contained two directly connected Zr_6 metal nodes with six

BTC ligands, where original formic acids at the node of MOF-808 metal node were replaced by two EDTA ligands.

Data availability

The data that support the plots within this paper and other findings of this study are available from the corresponding authors upon reasonable request. Source data are provided with this paper.

Received: 6 September 2020; Accepted: 9 July 2021;
Published online: 19 August 2021

References

1. McDonald, T. M. et al. Cooperative insertion of CO_2 in diamine-appended metal-organic frameworks. *Nature* **519**, 303–308 (2015).
2. Leung, J. J. et al. Solar-driven reduction of aqueous CO_2 with a cobalt *bis*(terpyridine)-based photocathode. *Nat. Catal.* **2**, 354–365 (2019).
3. Rao, H., Schmidt, L. C., Bonin, J. & Robert, M. Visible-light-driven methane formation from CO_2 with a molecular iron catalyst. *Nature* **548**, 74–77 (2017).
4. Wu, Y. A. et al. Facet-dependent active sites of a single Cu_2O particle photocatalyst for CO_2 reduction to methanol. *Nat. Energy* **4**, 957–968 (2019).
5. Ding, M., Flaig, R. W., Jiang, H. L. & Yaghi, O. M. Carbon capture and conversion using metal-organic frameworks and MOF-based materials. *Chem. Soc. Rev.* **48**, 2783–2828 (2019).
6. Appel, A. M. et al. Frontiers, opportunities, and challenges in biochemical and chemical catalysis of CO_2 fixation. *Chem. Rev.* **113**, 6621–6658 (2013).
7. Liu, X., Inagaki, S. & Gong, J. Heterogeneous molecular systems for photocatalytic CO_2 reduction with water oxidation. *Angew. Chem. Int. Ed.* **55**, 14924–14950 (2016).
8. Ji, Y. & Luo, Y. Theoretical study on the mechanism of photoreduction of CO_2 to CH_4 on the anatase TiO_2(101) surface. *ACS Catal.* **6**, 2018–2025 (2016).
9. Fu, Y. et al. An amine-functionalized titanium metal-organic framework photocatalyst with visible-light-induced activity for CO_2 reduction. *Angew. Chem. Int. Ed.* **51**, 3364–3367 (2012).
10. Li, D., Kassymova, M., Cai, X., Zang, S.-Q. & Jiang, H.-L. Photocatalytic CO_2 reduction over metal-organic framework-based materials. *Coord. Chem. Rev.* **412**, 213262 (2020).
11. White, J. L. et al. Light-driven heterogeneous reduction of carbon dioxide: photocatalysts and photoelectrodes. *Chem. Rev.* **115**, 12888–12935 (2015).
12. Wang, L. et al. Surface strategies for catalytic CO_2 reduction: from two-dimensional materials to nanoclusters to single atoms. *Chem. Soc. Rev.* **48**, 5310–5349 (2019).
13. Li, X., Yu, J., Jaroniec, M. & Chen, X. Cocatalysts for selective photoreduction of CO_2 into solar fuels. *Chem. Rev.* **119**, 3962–4179 (2019).
14. Corma, A. & Garcia, H. Photocatalytic reduction of CO_2 for fuel production: possibilities and challenges. *J. Catal.* **308**, 168–175 (2013).
15. Varghese, O. K., Paulose, M., LaTempa, T. J. & Grimes, C. A. High-rate solar photocatalytic conversion of CO_2 and water vapor to hydrocarbon fuels. *Nano Lett.* **9**, 731–737 (2009).
16. Guo, Z. et al. Selectivity control of CO versus $HCOO^-$ production in the visible-light-driven catalytic reduction of CO_2 with two cooperative metal sites. *Nat. Catal.* **2**, 801–808 (2019).
17. Wang, Y. et al. Visible-light driven overall conversion of CO_2 and H_2O to CH_4 and O_2 on 3D-SiC@2D-MoS_2 heterostructure. *J. Am. Chem. Soc.* **140**, 14595–14598 (2018).
18. Li, X. et al. Selective visible-light-driven photocatalytic CO_2 reduction to CH_4 mediated by atomically thin $CuIn_5S_8$ layers. *Nat. Energy* **4**, 690–699 (2019).
19. Long, R. et al. Isolation of Cu atoms in Pd lattice: forming highly selective sites for photocatalytic conversion of CO_2 to CH_4. *J. Am. Chem. Soc.* **139**, 4486–4492 (2017).
20. Zhao, Y. et al. Stable iridium dinuclear heterogeneous catalysts supported on metal-oxide substrate for solar water oxidation. *Proc. Natl Acad. Sci. USA* **115**, 2902–2907 (2018).
21. Wang, J.-W., Zhong, D.-C. & Lu, T.-B. Artificial photosynthesis: catalytic water oxidation and CO_2 reduction by dinuclear non-noble-metal molecular catalysts. *Coord. Chem. Rev.* **377**, 225–236 (2018).
22. Jiao, J. et al. Copper atom-pair catalyst anchored on alloy nanowires for selective and efficient electrochemical reduction of CO_2. *Nat. Chem.* **11**, 222–228 (2019).
23. Li, H. et al. Synergetic interaction between neighbouring platinum monomers in CO_2 hydrogenation. *Nat. Nanotechnol.* **13**, 411–417 (2018).
24. Furukawa, H., Cordova, K. E., O'Keeffe, M. & Yaghi, O. M. The chemistry and applications of metal-organic frameworks. *Science* **341**, 1230444 (2013).
25. Zhou, H. C. & Kitagawa, S. Metal-organic frameworks (MOFs). *Chem. Soc. Rev.* **43**, 5415–5418 (2014).
26. Li, B. et al. Emerging multifunctional metal-organic framework materials. *Adv. Mater.* **28**, 8819–8860 (2016).
27. Li, G., Zhao, S., Zhang, Y. & Tang, Z. Metal-organic frameworks encapsulating active nanoparticles as emerging composites for catalysis: recent progress and perspectives. *Adv. Mater.* **30**, e1800702 (2018).
28. Islamoglu, T. et al. Postsynthetic tuning of metal-organic frameworks for targeted applications. *Acc. Chem. Res.* **50**, 805–813 (2017).
29. Jiao, L., Wang, J. & Jiang, H.-L. Microenvironment modulation in metal-organic framework-based catalysis. *Acc. Mater. Res.* **2**, 327–339 (2021).
30. Medford, A. J. et al. From the Sabatier principle to a predictive theory of transition-metal heterogeneous catalysis. *J. Catal.* **328**, 36–42 (2015).
31. Guo, X. et al. Tackling the activity and selectivity challenges of electrocatalysts toward the nitrogen reduction reaction via atomically dispersed biatom catalysts. *J. Am. Chem. Soc.* **142**, 5709–5721 (2020).
32. Benkovic, S. J. & Hammes-Schiffer, S. A perspective on enzyme catalysis. *Science* **301**, 1196–1202 (2003).
33. Baek, J. et al. Bioinspired metal-organic framework catalysts for selective methane oxidation to methanol. *J. Am. Chem. Soc.* **140**, 18208–18216 (2018).
34. Kuhn, H. J., Braslavsky, S. E. & Schmidt, R. Chemical actinometry (IUPAC Technical Report). *Pure Appl. Chem.* **76**, 2105–2146 (2004).
35. Zhang, H. et al. Efficient visible-light-driven carbon dioxide reduction by a single-atom implanted metal-organic framework. *Angew. Chem. Int. Ed.* **55**, 14310–14314 (2016).
36. Yang, F. et al. Tuning internal strain in metal–organic frameworks via vapor phase infiltration for CO_2 reduction. *Angew. Chem. Int. Ed.* **132**, 4602–4610 (2020).
37. Qin, J.-S. et al. Creating well-defined hexabenzocoronene in zirconium metal–organic framework by postsynthetic annulation. *J. Am. Chem. Soc.* **141**, 2054–2060 (2019).
38. Mahmoud, M. E., Audi, H., Assoud, A., Ghaddar, T. H. & Hmadeh, M. Metal-organic framework photocatalyst incorporating *bis*(4′-(4-carboxyphenyl)-terpyridine)ruthenium(II) for visible-light-driven carbon dioxide reduction. *J. Am. Chem. Soc.* **141**, 7115–7121 (2019).
39. An, B. et al. Molecular iridium complexes in metal–organic frameworks catalyze CO_2 hydrogenation via concerted proton and hydride transfer. *J. Am. Chem. Soc.* **139**, 17747–17750 (2017).
40. Xu, H.-Q. et al. Visible-light photoreduction of CO_2 in a metal–organic framework: boosting electron–hole separation via electron trap states. *J. Am. Chem. Soc.* **137**, 13440–13443 (2015).
41. Chen, X. et al. MOFs conferred with transient metal centers for enhanced photocatalytic activity. *Angew. Chem. Int. Ed.* **59**, 17182–17186 (2020).
42. Hartmann, M., Azuma, N. & Kevan, L. Electron spin resonance and electron spin echo modulation study of Ni(I) in silicoaluminophosphate type 5: adsorbate interactions and evidence for the framework incorporation of Ni(I). *J. Phys. Chem.* **99**, 10988–10994 (1995).
43. Li, N. et al. Toward high-value hydrocarbon generation by photocatalytic reduction of CO_2 in water vapor. *ACS Catal.* **9**, 5590–5602 (2019).
44. Neatu, S., Macia-Agullo, J. A., Concepcion, P. & Garcia, H. Gold-copper nanoalloys supported on TiO_2 as photocatalysts for CO_2 reduction by water. *J. Am. Chem. Soc.* **136**, 15969–15976 (2014).
45. Yates, J. T. & Cavanagh, R. R. Search for chemisorbed HCO: the interaction of formaldehyde, glyoxal, and atomic hydrogen + CO with Rh. *J. Catal.* **74**, 97–109 (1982).
46. Koshland, D. E. Jr. & Neet, K. E. The catalytic and regulatory properties of enzymes. *Annu. Rev. Biochem.* **37**, 359–410 (1968).
47. Peng, Y. et al. A versatile MOF-based trap for heavy metal ion capture and dispersion. *Nat. Commun.* **9**, 187 (2018).
48. Furukawa, H. et al. Water adsorption in porous metal-organic frameworks and related materials. *J. Am. Chem. Soc.* **136**, 4369–4381 (2014).
49. Jrad, A., Abu Tarboush, B. J., Hmadeh, M. & Ahmad, M. Tuning acidity in zirconium-based metal organic frameworks catalysts for enhanced production of butyl butyrate. *Appl. Catal. A Gen.* **570**, 31–41 (2019).
50. VandeVondele, J. et al. Quickstep: fast and accurate density functional calculations using a mixed Gaussian and plane waves approach. *Comput. Phys. Commun.* **167**, 103–128 (2005).
51. Goedecker, S., Teter, M. & Hutter, J. Separable dual-space Gaussian pseudopotentials. *Phys. Rev. B* **54**, 1703–1710 (1996).
52. Nie, X., Esopi, M. R., Janik, M. J. & Asthagiri, A. Selectivity of CO_2 reduction on copper electrodes: the role of the kinetics of elementary steps. *Angew. Chem. Int. Ed.* **125**, 2519–2522 (2013).
53. Krack, M. & Parrinello, M. All-electron ab-initio molecular dynamics. *Phys. Chem. Chem. Phys.* **2**, 2105–2112 (2000).
54. Capdevila-Cortada, M. & Lopez, N. Entropic contributions enhance polarity compensation for CeO_2(100) surfaces. *Nat. Mater.* **16**, 328–334 (2017).
55. Clayborne, A., Chun, H. J., Rankin, R. B. & Greeley, J. Elucidation of pathways for NO electroreduction on Pt(111) from first principles. *Angew. Chem. Int. Ed.* **127**, 8373–8376 (2015).
56. Perdew, J. P., Burke, K. & Ernzerhof, M. Generalized gradient approximation made simple. *Phys. Rev. Lett.* **77**, 3865–3868 (1996).

57. Grimme, S., Antony, J., Ehrlich, S. & Krieg, H. A consistent and accurate ab initio parametrization of density functional dispersion correction (DFT-D) for the 94 elements H-Pu. *J. Chem. Phys.* **132**, 154104 (2010).
58. Nørskov, J. K. et al. Origin of the overpotential for oxygen reduction at a fuel-cell cathode. *J. Phys. Chem. B.* **108**, 17886–17892 (2004).
59. Peterson, A. A., Abild-Pedersen, F., Studt, F., Rossmeisl, J. & Nørskov, J. K. How copper catalyzes the electroreduction of carbon dioxide into hydrocarbon fuels. *Energy Environ. Sci.* **3**, 1311–1315 (2010).
60. Ling, C., Niu, X., Li, Q., Du, A. & Wang, J. Metal-free single atom catalyst for N_2 fixation driven by visible light. *J. Am. Chem. Soc.* **140**, 14161–14168 (2018).
61. Mills, G., Jdnsson, H. & Schenter, G. K. Reversible work transition state theory: application to dissociative adsorption of hydrogen. *Surf. Sci.* **324**, 305–337 (1995).
62. Henkelman, G., Uberuaga, B. P. & Jónsson, H. A climbing image nudged elastic band method for finding saddle points and minimum energy paths. *J. Chem. Phys.* **113**, 9901–9904 (2000).

Acknowledgements

This work was financially supported by the National Key Projects for Fundamental Research and Development of China (grant no. 2016YFB0600901 C.Z.), National Natural Science Foundation of China (grant nos. 22038010 to C.Z., 21978212 to H.H., 21725101 to H.L.J., 22161142001 to H.L.J., 91961119 to D.M. and 21521001 to H.L.J.) and the Science and Technology Plans of Tianjin (grant nos. 18PTSYJC00180 C.Z. and 19PTSYJC00020 H.H.). We thank the 1W1B station for X-ray absorption fine structure measurements at BSRF and Testing Centre of Tiangong University for providing some analytical tests.

Author contributions

C.Z. and H.L.J. conceived the idea, supervised and directed the project. H.L.J., J.L. and H.H. designed the study. J.L. and H.H. performed the experiments. W.X., X.S. and D.M. performed the theoretical calculations and analysed the DFT data. J.L. and K.S. conducted the DRIFTS and ESR experiments. C.W., L.N. and Y.L. participated in some experiments. C.L. and Y.P. studied the proton source in the photocatalytic product by synchrotron-radiation photoionization–mass spectrometry. J.L., H.H., H.L.J., K.S. and C.Z. cowrote the paper. All authors discussed the results and commented on the paper.

Competing interests

The authors declare no competing interests.

Additional information

Supplementary information The online version contains supplementary material available at https://doi.org/10.1038/s41929-021-00665-3.

Correspondence and requests for materials should be addressed to H.-L.J., D.M. or C.Z.

Peer review information *Nature Catalysis* thanks Julien Bonin, Mohamad Hmadeh and the other, anonymous, reviewer(s) for their contribution to the peer review of this work.

Reprints and permissions information is available at www.nature.com/reprints.

Publisher's note Springer Nature remains neutral with regard to jurisdictional claims in published maps and institutional affiliations.